Supplementary Information

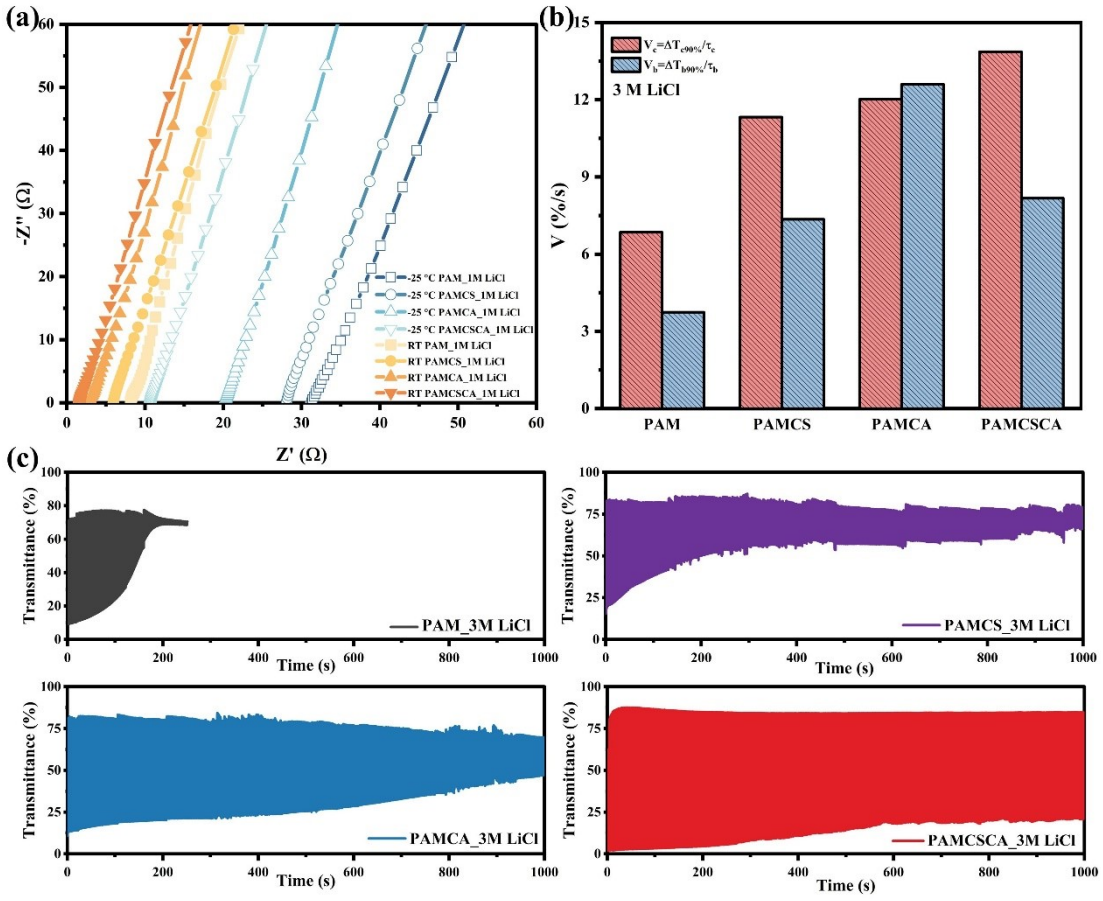

Fig. S1 (a) AC impedance spectra of gels with different polymer compositions at different temperature; (b) The electrochromic response rate of different gel substrates (V = ΔT/τ); (c) The cyclic stability of different gels.

To clarify the effects of CA and CMCS on the hydrogels, we prepared PAM, PAMCS, PAMCA, and PAMCSCA hydrogels under the same conditions for all other parameters. As shown in **Fig. S1a**, it can be seen that the intercept of the *x*-axis of PAMCSCA is the smallest, indicating the highest ionic conductivity, which suggests that the hydrogels, under the synergy of CA and CMCS, have improved performance. After assembling the gels into devices, since the devices assembled with different gels show different optical modulation amplitudes, for quantitative analysis, we defined the color change rate as the optical modulation amplitude divided by the response time. **Fig. S1b** shows the color change rate of the devices calculated, and it is obvious that the devices with CA and CMCS added exhibit a faster color change rate. Meanwhile,

Fig. S1c indicates that the devices with CA added have better cycling stability. It indicates that CMCS is introduced as a secondary polymer component to enhance the network structure and improve the water retention capacity through its hydrophilic main chain and abundant functional groups. CA is used as a multifunctional regulator, its multiple carboxyl groups combine with Li^+ to promote salt dissociation and ion transport, while improving the water retention capacity and freeze resistance.

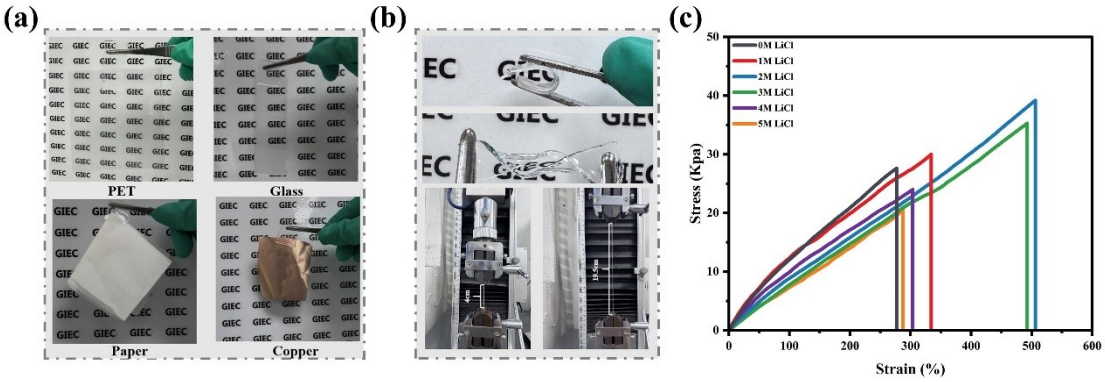

Fig. S2 (a) Adhesive property of the hydrogel to different materials, including PET, glass, paper and cupper; (b) Twisting and stretching ability of hydrogel; (c)Tensile Stress-strain profiles for PAM-CA-CMCS-x M LiCl (x=0-5).

Fig.S2(a) show the Adhesive property of the hydrogel to different materials. For different substrates, the adhesion of the PAMCSCA hydrogel arises from a combination of interfacial physicochemical interactions and, in some cases, mechanical interlocking. On glass substrates, surface silanol (Si–OH) groups can establish multivalent hydrogen-bonding interactions with the amide, carboxyl/carboxylate, and hydroxyl functionalities in the hydrogel network, promoting strong interfacial contact. On paper substrates, abundant cellulose –OH groups provide extensive hydrogen-bonding sites, and the hydrogel can partially infiltrate into the porous fiber network, generating additional mechanical interlocking that further improves adhesion. For plastic substrates, the adhesion is governed by surface polarity: polar plastics mainly interact with the hydrogel through hydrogen bonding and dipole–dipole interactions, whereas low-polarity plastics generally exhibit weaker interfacial interactions. For Cu metal substrates, the surface can interact with carboxyl/carboxylate and hydroxyl groups via

coordination/adsorption as well as hydrogen bonding, which enhances the interfacial affinity and contributes to the observed adhesive performance.

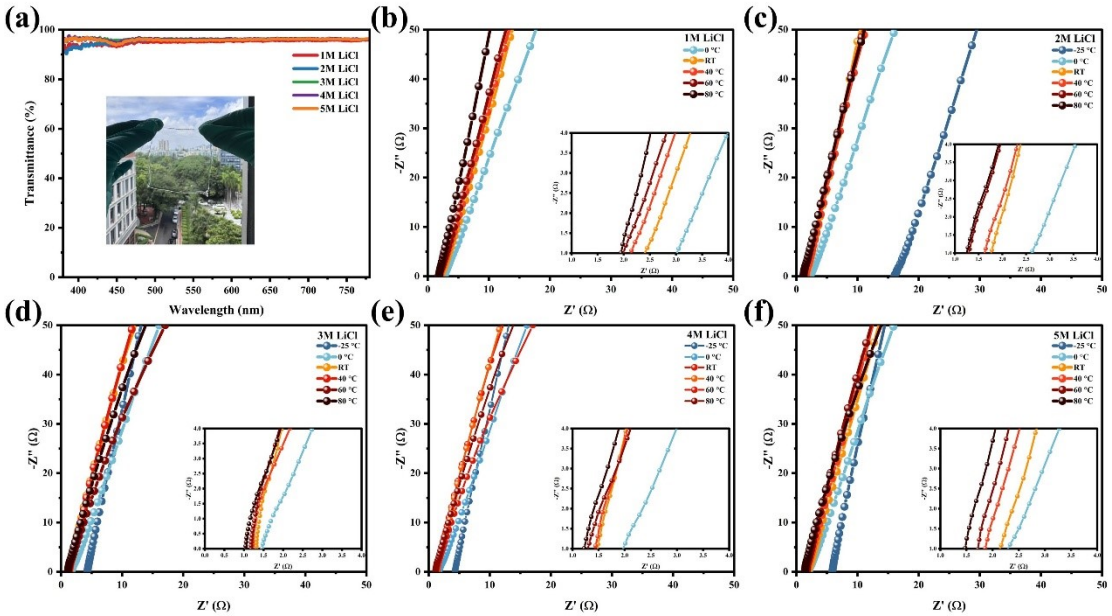

Fig. S3 (a) Transmittance spectra of the gels with different LiCl concentrations; (b-f) AC impedance spectra and ionic conductivity of gels with different LiCl concentrations at different temperatures.

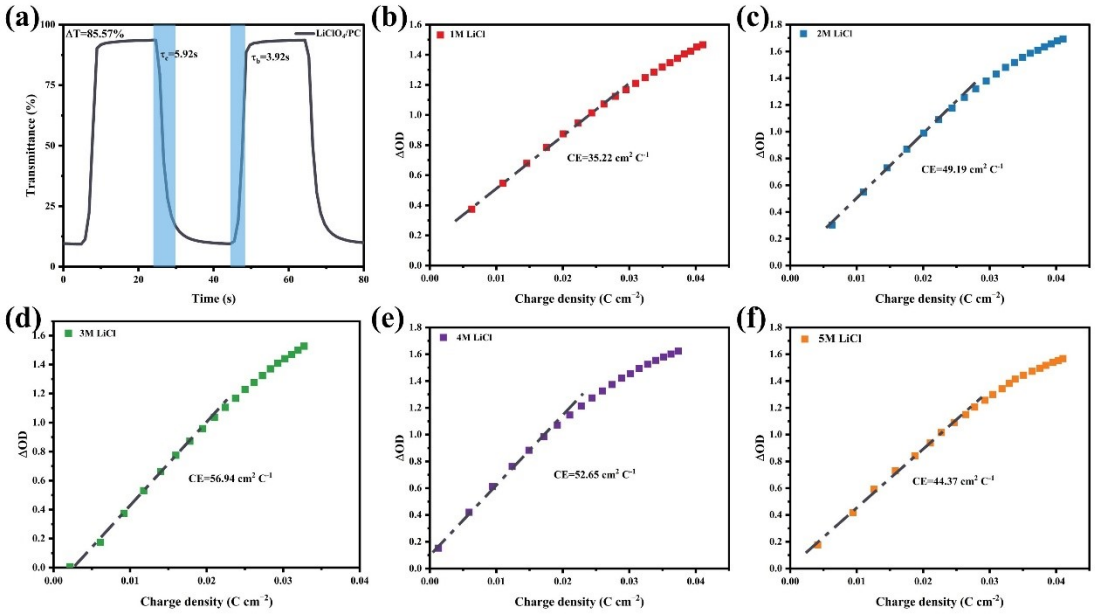

Fig. S4 (a) Transmission spectrum of the WO_3 films work in $LiClO_4$/PC at 633 nm between −1.0 V (20 s) to 1.0 V (20 s); (b-f) The coloration efficiency of ECDs with

1-5 M LiCl hydrogels.

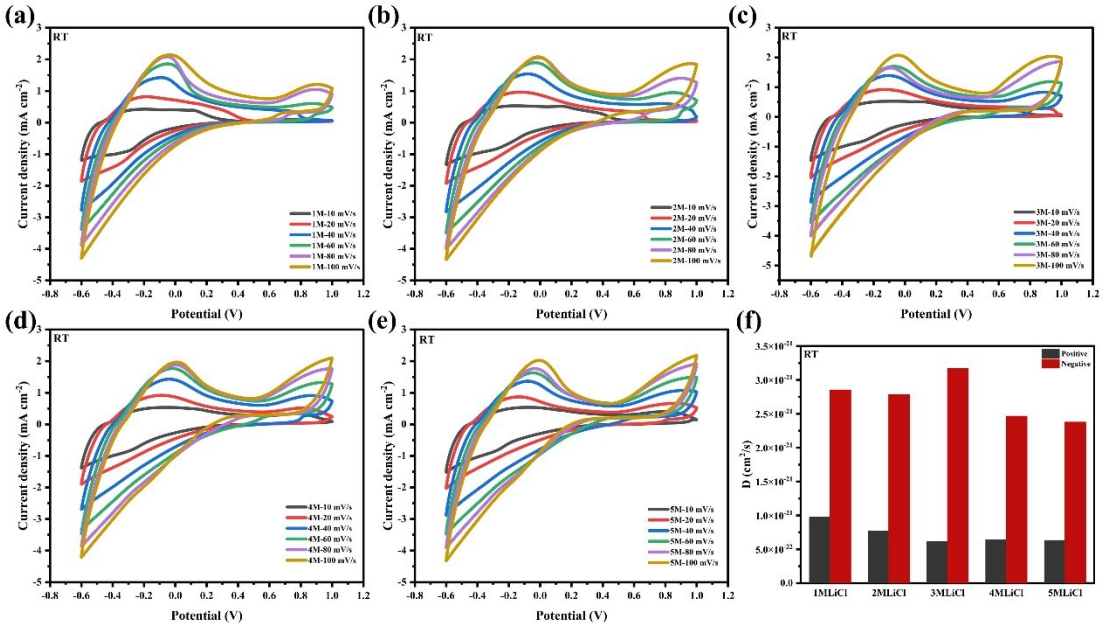

Fig. S5 (a-e) CV curves of ECDs with 1-5 M LiCl hydrogel at room temperature with different scan rates; (f) Calculated ion diffusion coefficient.

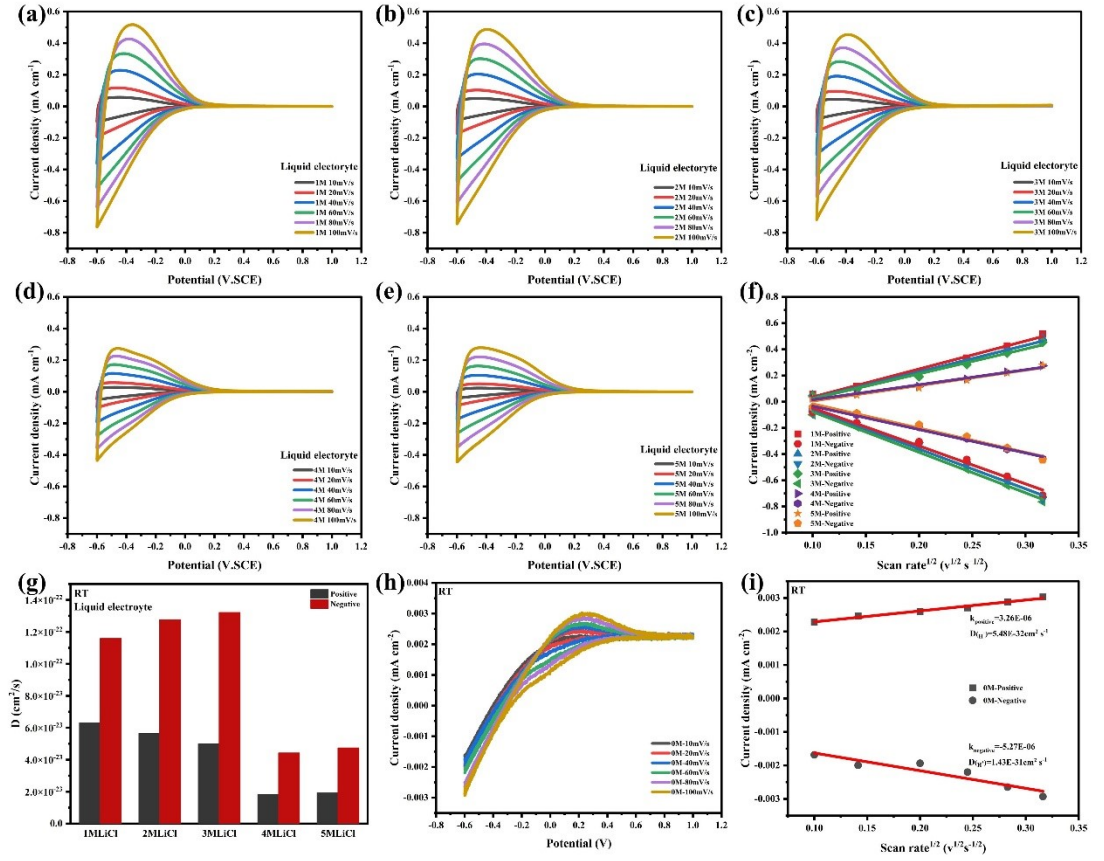

Fig. S6 (a-e) CV curves of WO_3 films in 1-5 M LiCl liquid electrolyte with different

scan rates; (f) The linear fitting relationship between the cathode (anode) peak current and the square root of the scan rate; (g) Calculated ion diffusion coefficient; (h) CV curves of ECDs with 0 M LiCl hydrogel at room temperature with different scan rates; (i) The linear fitting relationship between the cathode (anode) peak current and the square root of the scan rate.

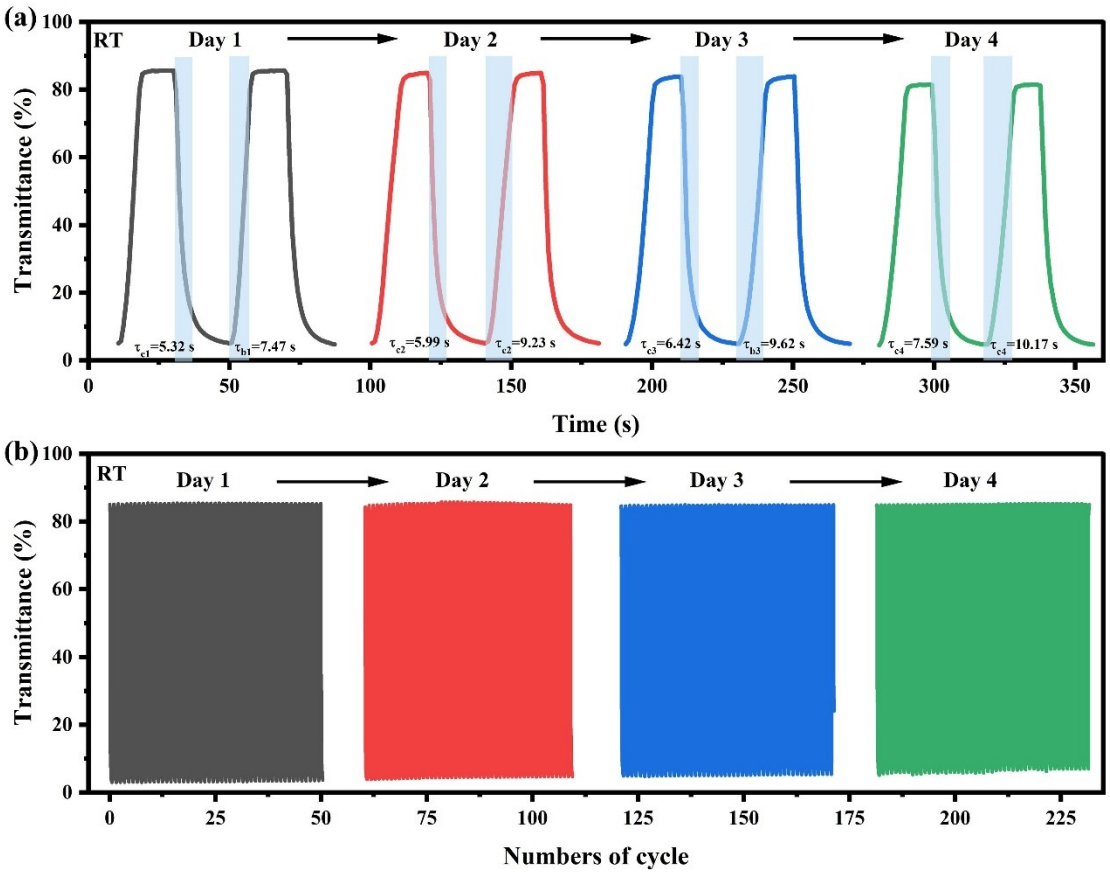

Fig. S7 Performance evolution of the electrochromic device after being stored in ambient air for 4 days. (a) Transmittance at 633 nm during CA cycling between -0.6 V (20 s) and 1.0 V (20 s); (b) Electrochromic cyclic stability

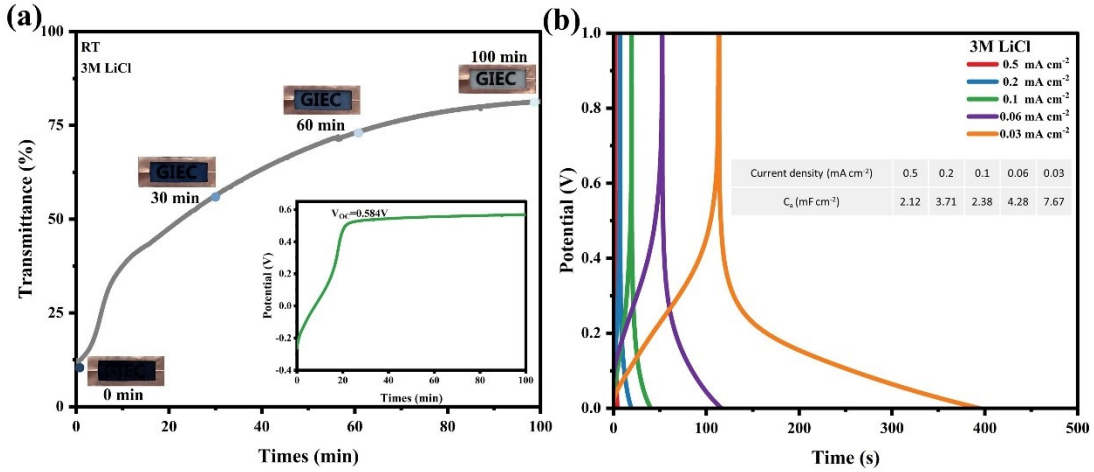

Current density (mA cm^{-2})	0.5	0.2	0.1	0.06	0.03
C_a (mF cm^{-2})	2.12	3.71	2.38	4.28	7.67

Fig. S8 (a) The Memory effect of 3 M ECDs, the inset is a curve of the open-circuit voltage over time during the self-bleached process; (b) GCD curves of 3 M ECDs under different current densities.

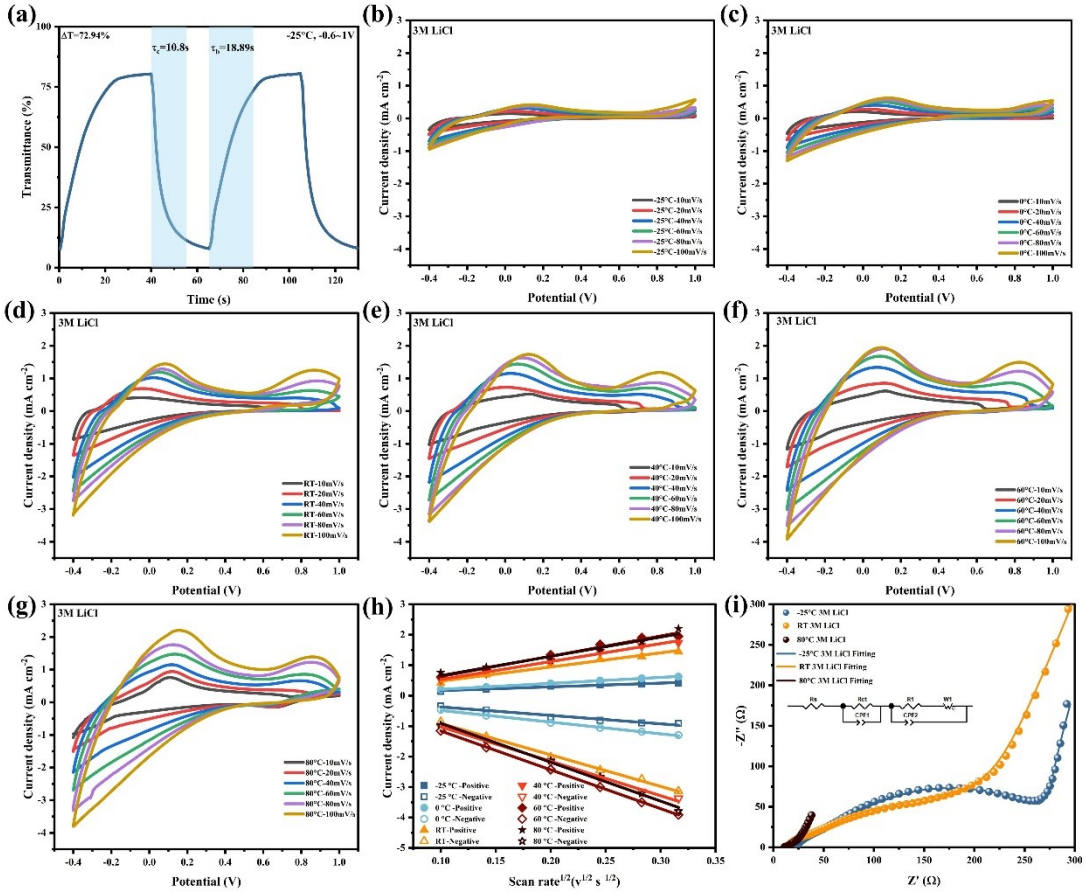

Fig. S9 (a)Transmission spectrum during the CA cycling process performed between −0.6 and 1.0 V of devices by 3 M LiCl at 633 nm at −25 °C; (b-g) CV curves at different temperature with different scan rates, (h) The linear fitting relationship between the cathode (anode) peak current and the square root of the scan rate; (i) AC impedance spectra of the ECDs at -25°C,RT and 80°C (the inset is the corresponding fitting equivalent circuit diagram).

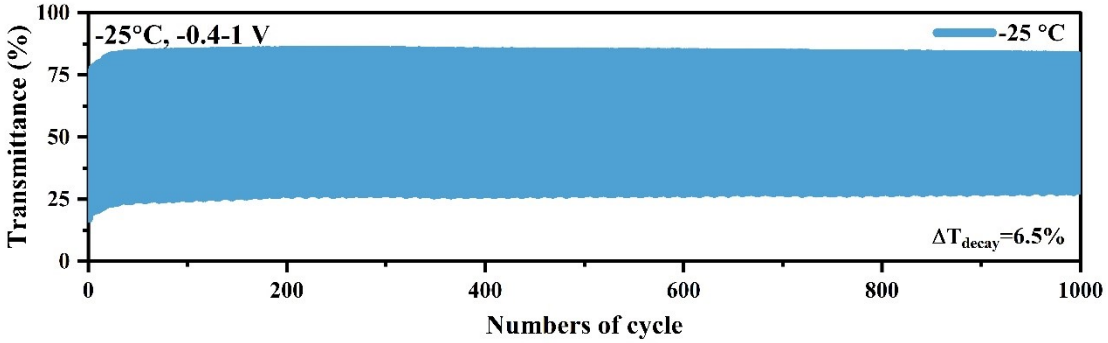

Fig. S10 Electrochromic cyclic stability at 630 nm between −0.4 V (40 s) ~ +1.0 V (30 s) for 1000 cycles.

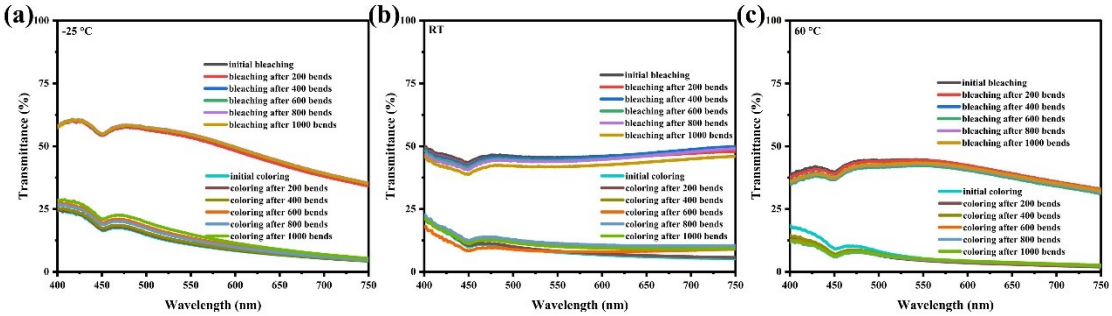

Fig. S11 Transmittance spectra of the flexible electrochromic device during coloration and bleaching for 1000 bending cycles at different temperatures (−25 °C in a refrigerator and 60 °C in an oven).

Fig. S12 Open-circuit voltage of crystalline silicon solar cells under indoor Low-light conditions

Table S1. Comparison of existing work and latest progress on ECDs using wide temperature range gel electrolytes (LT=Low temperature)

Electrochromic material	Electrolyte	RT Conductivity (mS/cm)	RT τ_c/τ_b	RT ΔT	LT Conductivity (mS/cm)	LT τ_c/τ_b	LT ΔT	Work temperature rage	Ref
$WO_3 \cdot xH_2O$ /PW	DES-LiTFSI	8.27 (20℃)	34s/15s	73% (633nm)	2.7 (-25℃)	--	30% (633nm)	-25℃-60℃	1
WO_{3-x}/Al	PVA-60wt% EG -Zn^{2+}-Al^{3+}	1.56	60s/46s	63% (633nm)	0.045 (-40℃)	--	20% (660nm)	-40℃-60℃	2
WO_{3-x}/Zn	PVA/EG–ZnCl2	12.5	12s/35s	62.3% (660nm)	1.25 (−40 °C)	90s/180s (-40 °C) 45s/90s (-25 °C)	45% (660nm)	-40℃-40℃	3
WO3/NiO	P(DEEA-co-IOBA)-NMA-LiTFSI	0.63 (30℃)	11.4s/8.4s	45% (700nm)	0.0522 (0 °C)	13.5s/20.2s (-25 °C)	--	-40℃-150℃	4

$WO_3 \cdot xH_2O$ /PANI	PVA/PAA-EG-H_2O	--	1.3s/1.1s	66.2% (600nm)	--	--	--	-20℃-60℃	[5]
PB/PBV	PAM/CCT-PEG -Glycerol-LiBr	28.8 (20°C)	2.7s/1.9s	65.1% (680nm)	11.0 (-40°C)	3.2s/2.8 s (-40 °C)	64% (680nm)	-40°C-60°C	[6]
PANI/ITO	PVDF-PC-$LiClO_4$	0.11	16.6s/15.5s	40% (550nm)	--	14s/--	5% (550nm)	-10°C-60°C	[7]
WO_3/Cu	PAM/CA/CMCS -3MLiCl	17.91	4.69s/10.4s	86.01% (633nm)	6.12 (-25°C)	10.08s/18.9s (-25 °C)	73% (630nm)	-25°C-80°C	This work

Ref:

1 M. Ma, S. Jia, C. Bian, W. Yang, Y. Zhong, J. Ma and G. Cai, *Advanced Functional Materials*, **n/a**, e20971.

2 B. Qiu, X. Xiao, G. Xu and G. Dong, *Materials Today Chemistry*, 2023, **33**, 101703.

3 W. Wu, H. Fang, L. Wu, H. Ma and H. Wang, *ACS Applied Materials & Interfaces*, 2023, **15**, 4113-4121.

4 P. Sun, J. Chen, Y. Li, X. Tang, H. Sun, G. Song, X. Mu, T. Zhang, X. Zha, F. Li, Y. Gao, S. Cong and Z. Zhao, *InfoMat*, 2023, **5**, e12363.

5 Q. Li, J. Li, W. Wang, D. Ma, G. Li and J. Wang, *Advanced Functional Materials*, 2025, **35**, 2415874.

6 X. Li, N. Ma, G. Xu, R. Zhang and J. Liu, *Solar Energy Materials and Solar Cells*, 2022, **234**, 111449.

7 H. Gong, A. Li, G. Fu, M. Zhang, Z. Zheng, Q. Zhang, K. Zhou, J. Liu and H. Wang, *Journal of Materials Chemistry A*, 2023, **11**, 8939-8949.